Theoretical investigation on thermoelectric properties of Cu-based chalcopyrite compounds

Biao Wang,[1,2] Hongjun Xiang,[3] Tsuneyoshi Nakayama,[1,4] Jun Zhou,[1,*] and Baowen Li[2]
[1]*Center for Phononics and Thermal Energy Science, School of Physics Science and Engineering, Tongji University, 200092 Shanghai, People's Republic of China*
[2]*Department of Mechanical Engineering, University of Colorado, Boulder, Colorado 80309, USA*
[3]*Key Laboratory of Computational Physical Sciences (Ministry of Education), State Key Laboratory of Surface Physics, and Department of Physics, Fudan University, 200433 Shanghai, People's Republic of China*
[4]*Hokkaido University, Sapporo 060-0826, Japan*
(Received 12 October 2016; revised manuscript received 6 December 2016; published 3 January 2017)

Cu-based materials are potential candidates for commercial thermoelectric materials due to their abundance, nontoxicity, and high performance. We incorporate the multiband Boltzmann transport equations with first-principles calculations to theoretically investigate the thermoelectric properties of Cu-based chalcopyrite compounds. As a demonstration of our method, the thermoelectric properties of quaternary compounds Cu_2ZnSnX_4 (X = S, Se) and ternary compounds $CuBTe_2$ (B = Ga, In) are studied. We systematically calculate the electrical conductivity, the Seebeck coefficient, and the power factor of the four materials above based on parameters obtained from first-principles calculations and using several other fitting parameters. For quaternary compounds, our results reveal that $Cu_2ZnSnSe_4$ is better than Cu_2ZnSnS_4 and its optimal hole concentration is around 5×10^{19} cm^{-3} with the peak power factor 4.7 μW/cm K^2 at 600 K. For ternary compounds, we find that their optimal hole concentrations are around 1×10^{20} cm^{-3} with the peak power factors over 26 μW/cm K^2 at 800 K.

DOI: 10.1103/PhysRevB.95.035201

I. INTRODUCTION

Thermoelectric (TE) devices are solid-state energy converters used for power generation and/or TE cooling [1,2]. For widespread use of TE devices, the devices need to improve their efficiency over conventional energy converters. The energy conversion efficiency of TE materials is characterized by a dimensionless figure of merit $ZT = \sigma S^2 T/\kappa$, where σ is the electrical conductivity, S is the Seebeck coefficient, T is the absolute temperature, and κ is the thermal conductivity consisting of electronic and lattice thermal conductivities. The performance of $ZT \geqslant 1$ is preferable to gain high-energy conversion efficiency. The commonly used BiSbTe alloy belongs to this category whose ZT value is around 1 near room temperature [3], and it is possible to improve its value further to 1.4 by introducing nanostructures [4]. PbTe-based materials and SiGe alloy have been also known to take $ZT > 1$, which are widely used for waste heat harvesting and power generation in mid- and high-temperature regimes, respectively. The mass production of these materials is restricted because the elements Pb and Ge are toxic and expensive. A larger power factor (PF), defined as σS^2, is also required to gain larger output power.

In recent years, Cu-based materials have been proposed as a new class of TE materials because of their low price and nontoxicity [5]. Usually, Cu-based materials can be categorized into four classes. (i) The first class is Cu-based diamond-like compounds, including ternary and quaternary compounds. In-doped Cu_2SnSe_3 is reported to possess ZT of around 1.14 at 850 K [6]. The reported ZT values of undoped $CuInTe_2$ (CIT) [7] and $CuGaTe_2$ (CGT) [8] are 1.18 at 850 K and 1.4 at 950 K, respectively. $Cu_2ZnSnSe_4$ (CZTSe) and Cu_2ZnSnS_4 (CZTS) are also potential Cu-based TE materials which have been studied both experimentally and theoretically [9–13]. Very recently, the ZT value of Cu-doped CZTSe has been found to be 0.70 at 450 °C [14]. Because of the wide band gaps (usually larger than 1 eV) of these materials, the bipolar effect which may reduce the TE efficiency can be suppressed effectively. Inspired by many chalcopyrite structure compounds, Zhang *et al.* [15] developed a pseudocubic structure approach to search for high-performance TE materials. (ii) The second class is Cu-based superionic conductors, such as liquid-like $Cu_{2-x}Se$ and $Cu_{2-x}S$, which bring a new concept termed "phonon-liquid electron-crystals" [16,17] to improve TE performance. In the superionic phase, ultralow thermal conductivity is found because the mobile Cu ions suppress the transverse phonon modes. (iii) The third class is called "tetrahedrites", such as $Cu_{12}Sb_4S_{13}$. They are qualified as promising TE materials because of their complex crystal structures (58 atoms in unit cell) and highly symmetric crystal structure [18]. The maximum ZT reported in tetrahedrite materials so far is around 1 at 700 K [19–21]. (iv) The fourth class is oxyselenide BiCuSeO, whose TE properties were first investigated by Zhao *et al.* in 2010 [22]. ZT values above 1 have been reported in Pb-doped and Ba-doped BiCuSeO [23–25]. It has been recognized that there are two challenges for Cu-based TE materials to overcome: one is the lack of n-type materials and the second is the severe migration of Cu ions under large electric current or heat current [26]. Compared to conventional TE materials, the material properties and transport properties of Cu-based materials are not well understood. In order to maximize ZT, parameters such as carrier concentration, effective mass, band gap, etc., must be optimized [27].

In this paper, the multiband Boltzmann transport equations (BTEs) are used to explore and predict the TE transport

*zhoujunzhou@tongji.edu.cn

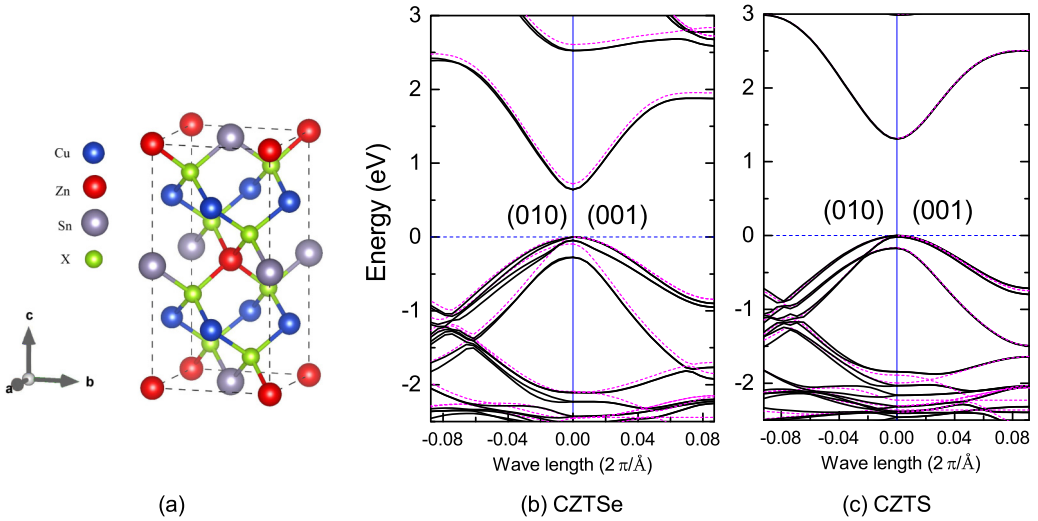

FIG. 1. (a) Crystal structure of stannite CZTX. Calculated band structures of stannite CZTSe (b) and CZTS (c); the k-point path is along the (010) and (001) directions near the Γ point. The band structures without SOC are shown by dashed lines.

properties. The parameters such as band gap and effective mass of each band are calculated from first-principles calculations to solve the BTEs. The relaxation time approximation (RTA) based on the multiband carrier transport model [28] is also used. In order to demonstrate our method, we study the TE properties of the p-type Cu-based quaternary chalcopyrite CZTX (X = S, Se) and ternary chalcopyrite $CuBTe_2$ (CBT; B = Ga, In). Based on these results, the optimal carrier concentrations for peak PF are predicted for the above four Cu-based materials. The TE properties of other Cu-based materials can be studied similarly.

II. BAND STRUCTURES

We employ the VASP package [29] within the Perdew-Burke-Ernzerhof (PBE) form of the generalized gradient approximation (GGA) [30] to calculate the band structures of Cu-based TE materials. We are aware of the difference among the calculated band structures by using different methods such as PBE, PBE+U, the modified Becke-Johnson potential (MBJ), MBJ+U, etc. [31]. However, the main objective of this paper is not to compare these methods but to calculate the transport properties. Therefore, only the results from PBE are presented. For GGA pseudopotentials, the valence configurations of the constituent atoms are chosen as Cu($3d^{10}4p^1$), Zn($3d^{10}4p^2$), Sn($4d^{10}5s^2p^2$), S($3s^2p^4$), Se($4s^2p^4$), Ga($3d^{10}4s^2p^1$), In($4d^{10}5s^2p^1$), and Te($5s^2p^4$). We choose the standard Heyd-Scuseria-Ernzerhof (HSE06) hybrid functional [32,33] with the screening parameter set to 0.2 Å for the exchange-correlation potential since Cu-d electrons play an important role in electronic properties of Cu-based multinary semiconductors [34]. The projector augmented wave (PAW) pseudopotentials [35] with an energy cutoff of 400 eV for the plane wave basis and 5 × 5 × 5 Monkhorst-Pack [36] Γ-centered k-point meshes were employed. We take the spin-orbit coupling (SOC) into account in these calculations since the SOC strongly affects the effective mass tensor even in light materials [37].

A. CZTX

Figure 1 shows the crystal structure and the calculated band structure of stannite CZTX. a,b,c are the lattice constants along the x, y, z directions, respectively, as shown in Fig. 1(a). The space group of stannite CZTX is $I\bar{4}2m$. The main results are summarized in Table I, which will be basic input parameters for calculating TE properties in the next section. The results are compared with the values reported in Refs. [38,39] to assure the accuracy of our calculations. We find that the calculated lattice constants a, tetragonal distortion parameter ($\eta = c/2a$), and band gaps (E_g) are in agreement with the values in Ref. [39]. Moreover, the conduction band minimum (CBM), which is noted as $E^0_{i,e}$ with conduction band index $i = 1,2,\ldots$, and the valence band maximum (VBM), which is noted as $-E^0_{i,h}$ with valence band index i, are located at the Γ point, indicating direct band gaps. Therefore, the band

TABLE I. The lattice constants a, the tetragonal distortion parameters $\eta = c/2a$, and band gaps of stannite CZTX and CBT. VBMs ($-E_{i,0}$) of three topmost valence bands are presented. The values in parentheses give corresponding results from Ref. [39] for CZTX, Ref. [8] for CGT, and Ref. [40] for CIT.

	a (Å)	η	E_g (eV)	$-E^0_{1,h}$ (eV)	$-E^0_{2,h}$ (eV)	$-E^0_{3,h}$ (eV)
CZTSe	5.709 (5.712)	1.007 (1.006)	0.642 (0.64)	0	−0.047	−0.276
CZTS	5.428 (5.429)	1.007 (1.007)	1.308 (1.30)	0	−0.018	−0.171
CGT	6.064 (6.016)	0.992 (0.993)	1.072 (1.2)	0	−0.035	−0.751
CIT	6.253 (6.196)	1.002 (1.003)	0.773 (1.04)	0	−0.014	−0.713

TABLE II. Effective masses of the lowest conduction band and three topmost valence bands along the ∥ axis and along the ⊥ axis in CZTX and CBT. All numerical values are in units of the free electron mass (m_0).

(i,j)	CZTSe ∥	CZTSe ⊥	CZTS ∥	CZTS ⊥	CGT ∥	CGT ⊥	CIT ∥	CIT ⊥
$(1,e)$	0.101	0.092	0.176	0.186	0.094	0.093	0.075	0.083
$(1,h)$	0.203	0.536	0.454	0.748	0.291	0.102	0.213	0.380
$(2,h)$	0.180	0.152	0.685	0.701	0.116	0.318	0.104	0.092
$(3,h)$	0.275	0.176	0.366	0.205	0.288	0.303	0.281	0.283

gaps (E_g) are 0.642 eV for CZTSe and 1.308 eV for CZTS, respectively. The lowest conduction band and three topmost valence bands are taken into account in our BTE calculations.

Figures 1(b) and 1(c) show that the valence bands are split due to the effect of crystal field and SOC [39] both in CZTSe and CZTS. Corresponding band structures in the absence of SOC are also shown in the figure. We find that two topmost valence bands are slightly changed by SOC and the third topmost valance band is shifted to higher energy in CZTSe. Moreover, the SOC effect is not obvious in CZTS because the S atom is much lighter than the Se atom. By setting the VBM of the highest valence band ($-E^0_{1,h}$) to be zero, the VBMs of other two valence bands, $-E^0_{2,h}$ and $-E^0_{3,h}$, are -0.047 eV (-0.018 eV) and -0.276 eV (-0.171 eV) for CZTSe (CZTS). All these three valence bands should be incorporated in the hole transport calculation since they are close enough. The effective mass tensor of band i,j, where $j=(e,h)$ representing the electrons and holes, can be written as

$$\frac{1}{m^*_{i,j}} = \begin{pmatrix} m^{*-1}_{\perp,i,j} & 0 & 0 \\ 0 & m^{*-1}_{\perp,i,j} & 0 \\ 0 & 0 & m^{*-1}_{\parallel,i,j} \end{pmatrix}. \quad (1)$$

There are two independent components in effective mass tensor: the longitudinal effective mass $m^*_{\parallel,i,j}$ along the c axis and the transverse effective mass $m^*_{\perp,i,j}$ along the a and b axes, where $m^{*-1}_{\parallel,i,j} = \frac{1}{\hbar^2}\frac{\partial^2 E_{i,j}}{\partial k_z^2}$ and $m^{*-1}_{\perp,i,j} = \frac{1}{\hbar^2}\frac{\partial^2 E_{i,j}}{\partial k_x^2} = \frac{1}{\hbar^2}\frac{\partial^2 E_{i,j}}{\partial k_y^2}$. Here $E_{i,j}$ is the energy and $k_{x,i,j}$, $k_{y,i,j}$, $k_{z,i,j}$ are wave vector components. $\hbar$ is the Plank constant. We fit the band structure of each VBM and CBM to obtain the corresponding effective mass near the Γ point. Table II shows the effective mass of the conduction band (electrons) and the three topmost valance bands (holes) along the longitudinal and transverse directions in CZTX. The electron and hole masses in CZTSe are lighter than the effective masses in CZTS.

B. CBT

The crystal structure of $CuBTe_2$ is shown in Fig. 2(a). The space group is $I\bar{4}2d$. Figures 2(b) and 2(c) show the band structures of CGT and CIT, respectively. Table I lists the parameters of CGT and CIT obtained from first-principles calculations in comparison with the experimental data extracted from Ref. [8] and Ref. [40]. The calculated lattice constants are in good agreement with the experimental data. A direct band gap is confirmed at the Γ point with a slightly underestimated energy gap compared to the experimental measurements. Similarly to quaternary chalcopyrite, the three topmost valence bands and the lowest conduction band near the Γ point are taken into account. It has been pointed out that the major contribution to the bands near the VBM comes from the Cu-d states and Te-p states [41]. By considering the strong SOC originated from heavy Te atoms, the third highest valence band is far below the highest valence band in both compounds, $-E^0_{3,h} = -0.751$ eV for CGT and $-E^0_{3,h} = -0.713$ eV for CIT. Such strong effect of SOC can be confirmed by comparing the band structures with and without SOC in Fig. 2. As a result, the third highest valence band contributes marginally to transport properties in the above materials, which is detrimental to high TE performance [42]. The longitudinal and transverse effective masses of CGT and CIT are obtained by fitting the band structure near the Γ point. The fitted values are shown in Table II. We found that holes in those ternary Cu-based compounds are lighter than the holes in quaternary Cu-based compounds. The heaviest holes are less than $0.4m_0$; in comparison the heaviest values in quaternary Cu-base materials are about $0.7m_0$. Therefore, the TE performance of CIT and CGT could be better than the TE performance of CZTS and CZTSe.

III. THERMOELECTRIC TRANSPORT PROPERTIES

Under the framework of the BTE with RTA, we consider electrical carrier transport in multiple energy bands with the Kane model [43]. In other words, we assume the TE transport of electrical carriers in both the lowest conduction bands and the highest valence bands; each of these bands is considered to be twofold degenerate due to spin degeneracy. Taking the nonparabolicity into account, the dispersion relation of each band is

$$\sum_\xi \frac{\hbar^2 k^2_{\xi,i,j}}{2m^*_{\xi,i,j}} = \gamma(E_{i,j}) = E_{i,j} + \frac{E^2_{i,j}}{E_g}. \quad (2)$$

Here ξ represents ∥ and ⊥. $k_\perp = (k_x^2 + k_y^2)^{1/2}$ and $k_\parallel = k_z$. $m^*_{d,i,j} = (m^{*2}_{i,j,\perp} m^*_{i,j,\parallel})^{1/3}$ is noted as the density-of-states effective mass of each band. The doping concentration n equals the difference between the concentration of holes (n_h) and the concentration of electrons (n_e). Thus, the chemical potential μ in p-type materials with a fixed n can be determined by [44]

$$\begin{aligned} n &= n_h - n_e \\ &= \sum_i \frac{\sqrt{2} m^{*3/2}_{d,i,h}}{\pi^2\hbar^3} \int_0^\infty \gamma^{1/2}(E_{i,h})\gamma'(E_{i,h}) \\ &\quad \times \frac{1}{\exp\left[\left(E_{i,h} + E^0_{i,h} + \mu\right)/k_B T\right] + 1} dE_{i,h} \\ &\quad - \sum_i \frac{\sqrt{2} m^{*3/2}_{d,i,e}}{\pi^2\hbar^3} \int_0^\infty \gamma^{1/2}(E_{i,e})\gamma'(E_{i,e}) \\ &\quad \times \frac{1}{\exp\left[\left(E_{i,e} + E_g + E^0_{i,e} - \mu\right)/k_B T\right] + 1} dE_{i,e}. \end{aligned} \quad (3)$$

Here $\gamma'(E_{i,j}) = 1 + 2E_{i,j}/E_g$ and k_B is the Boltzmann constant.

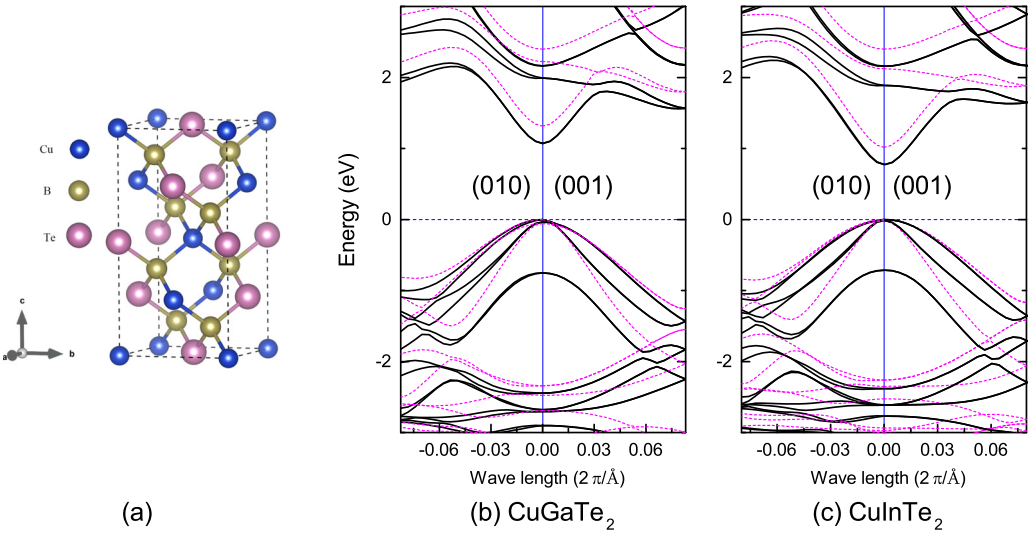

FIG. 2. (a) Crystal structure of CuBT. Calculated band structures of CGT (b) and $CuInTe_2$ (c); the k-point path is along the (010) and (001) directions near the Γ point. The band structures without SOC are shown by dashed lines.

The TE transport coefficients can then be calculated by solving BTE under RTA. The electrical conductivity along direction ξ (σ_ξ) and the Seebeck coefficient along direction ξ (S_ξ) can be written as [28]

$$\sigma_\xi = \sum_{i,j} \sigma_{\xi,i,j}, \quad S_\xi = \frac{\sum_{i,j} S_{i,j}\sigma_{\xi,i,j}}{\sum_{i,j} \sigma_{\xi,i,j}}, \tag{4}$$

where the definitions are

$$\sigma_{\xi,i,j} = \frac{q_j^2}{3\pi^2 m^*_{\xi,i,j}} \left(\frac{2k_B T m^*_{d,i,j}}{\hbar^2}\right)^{3/2} L^0_{i,j}, \tag{5}$$

$$S_{i,j} = \frac{k_B}{q_j}\left(\frac{L^1_{i,j}}{L^0_{i,j}} - \Omega_{i,j,F}\right). \tag{6}$$

The dimensionless transport coefficient is defined as

$$L^n_{i,j}(T) = \int_0^\infty \Omega^n_{i,j}\gamma^{3/2}(\Omega_{i,j})\tau_{i,j}\left(-\frac{\partial f_0}{\partial \Omega_{i,j}}\right)d\Omega_{i,j}. \tag{7}$$

In the above, q_j is the charge of carrier, $\Omega_{i,j} = E_{i,j}/k_BT$, $\Omega_{i,e,F} = (\mu - E_g - E_{i,e,0})/k_BT$, $\Omega_{i,h,F} = (-\mu - E_{i,h,0})/k_BT$, $\Omega_g = E_g/k_BT$, $\gamma(\Omega_{i,j}) = \Omega_{i,j}(1 + \Omega_{i,j}/\Omega_g)$, and f_0 is the Fermi-Dirac distribution. $\tau_{i,j}$ is the total relaxation time which can be calculated by the Mathiessen's rule while assuming that the scattering events are independent of each other:

$$\frac{1}{\tau_{i,j}} = \frac{1}{\tau^{imp}_{i,j}} + \frac{1}{\tau^{po}_{i,j}} + \sum_l \frac{1}{\tau^{da,l}_{i,j}} + \sum_{l'} \frac{1}{\tau^{do,l'}_{i,j}}, \tag{8}$$

where $\tau^{imp}_{i,j}$ is the relaxation time from carrier-impurity scattering, $\tau^{po}_{i,j}$ is from carrier-longitudinal polar optical phonon scattering, $\tau^{da,l}_{i,j}$ is from carrier-deformation acoustic phonon scattering, and $\tau^{do,l'}_{i,j}$ is from carrier-deformation optical phonon scattering, where l (l') denotes the different branches of deformation acoustic (optical) phonon. In principle, the relaxation time for different scattering mechanisms can be obtained by using the Fermi's golden rule. The detailed temperature- and energy-dependent expressions for each scattering relaxation time mentioned above can be found in Refs. [28,43].

A. TE properties of CZTX

We now turn to calculate the electrical conductivity and the Seebeck coefficient of p-type stannite CZTX based on the band structures of CZTX obtained from first-principles calculations in Sec. II A. The lowest conduction band and three valence bands near Γ point are taken into account in our calculations where the spin degeneracy of each band is also considered. In these p-type wide band gap semiconductors, the bipolar effect is weak and holes dominate the transport properties. In order to justify the input parameters in our calculation, we first fit the experimental data of CZTSe reported by Liu *et al.* in Ref. [9]. The isotropic electrical conductivity along different directions is averaged to compare to the measured electrical conductivity.

Figure 3 shows that the calculated electrical conductivities and the Seebeck coefficients as a function of temperature are in good agreement with the experimental results. Table III presents the reasonable fitted parameters adopted in our calculations. We find that the electrical conductivity of CZTSe is much lower than the electrical conductivity of the state-of-the-art BiSbTe alloy which is above 1000 S/cm at room temperature and 600 S/cm at 450 K [4]. A decrease of electrical conductivity with increasing temperature comes from the enhancement of scattering strength at higher temperature. As for the Seebeck coefficient, its absolute value increases with increasing temperature while the bipolar effect is negligible. Some of the fitting parameters are compared to the values from other theories. The optical phonon energy and the high-frequency permittivity are within the range of values from first-principles calculations in Ref. [45] and in Ref. [38], respectively.

We further explore the carrier concentration dependence of the TE properties of CZTSe using the fitted parameters to find the optimal concentration. The TE properties of CZTS are also calculated. In order to simplify the calculations,

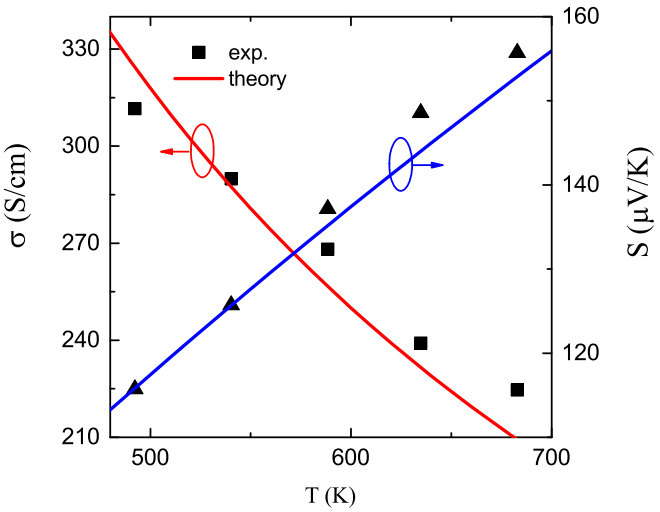

FIG. 3. Calculated electrical conductivity (a) and Seebeck coefficient (b) of CZTSe as a function of temperature. The experimental data are extracted from Ref. [9].

we assume that several parameters of CZTS such as the optical phonon energy, permittivities, deformation potential constants, and sound velocity are the same as the parameters of CZTSe. Figure 4 shows the electrical conductivity, Seebeck coefficient, and power factor (PF) versus hole concentration at 500 K, 600 K, and 700 K. Figure 4(a) clearly shows that σ increases with increasing hole concentration and with decreasing temperature for both CZTSe and CZTS. The reason is $\sigma \propto n_h$ and $\sigma \propto \tau \propto 1/T$. The electrical conductivity of CZTSe is significantly larger than that of CZTS because the effective mass of CZTSe is smaller as shown in Table II. Figure 4(b) shows that the Seebeck coefficients decrease with increasing hole concentration and with increasing temperature for both CZTSe and CZTS. The main reason is that the chemical potential shifts to higher energy for smaller hole concentration and higher temperature. We can also see that the Seebeck coefficient of CZTSe is smaller than that of CZTS because of the smaller effective mass. Figure 4(c) presents the PF of CZTSe and CZTS. The PF of CZTSe

TABLE III. Fitting parameters used to calculate the transport coefficients in CZTX. The values in parentheses are the parameters of CZTS when they are different from that of CZTSe.

Parameters	Fitted value	Reference
n (cm^{-3})	6.25×10^{19}	6.25×10^{19}[a]
impurity density (cm^{-3})	3×10^{19}	
mass density (g cm^{-3})	5.68 (4.35)	5.68 (4.35)[b]
optical phonon energy (meV)	16.2	7.44 ∼ 44[c]
deformation potential constant (eV)	6.5	
static permittivity (ϵ_0)	80	
high-frequency permittivity (ϵ_0)	8.2	8.2 ∼ 9.0[d]
sound velocity (m/s)	3000	

[a]Reference [9].
[b]Landolt-Börnstein database.
[c]Reference [45].
[d]Reference [38].

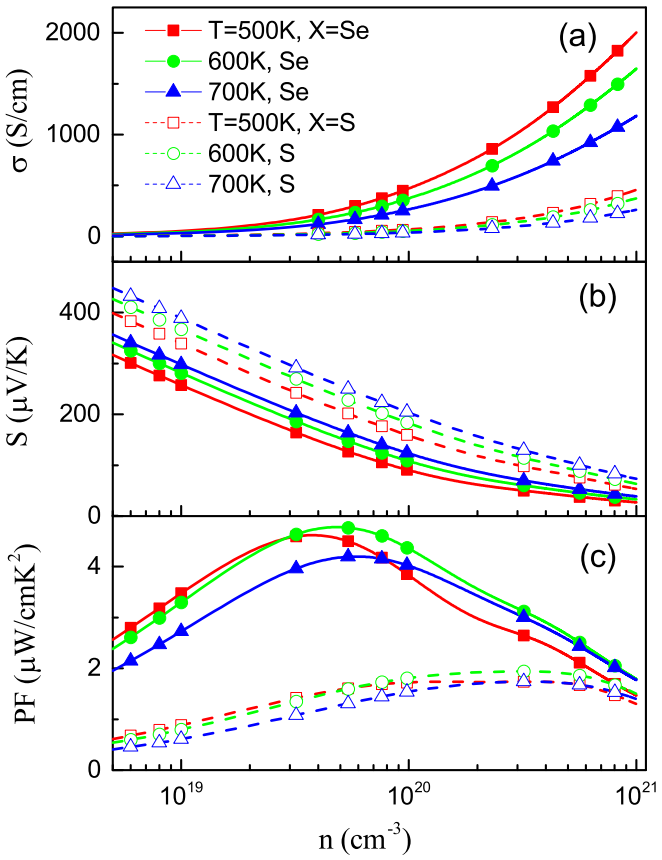

FIG. 4. Calculated electrical conductivity (a), Seebeck coefficient (b), and power factor (c) versus carrier concentration in CZTSe and CZTS at $T = 500$ K, 600 K, 700 K.

is always larger than the PF of CZTS. A maximum PF of CZTSe of 4.8 μW/cm K^2 can be found when the hole concentration is about 5×10^{19} cm^{-3} and $T = 600$ K. The optimal hole concentration of CZTS is around 4×10^{20} cm^{-3} with maximum PF 1.6 μW/cm K^2 when $T = 600$ K. We point out that CZTSe is more advantageous and favorable than CZTS for TE applications. The thermal conductivity of CZTSe is reported less than 1 W/mk at 700 K [9,12,14], which leads to a ZT value of around 0.29 for CZTSe at 700 K.

B. TE properties of CBT

The lowest conduction band and the three topmost valence bands are also taken into account in the calculation of CBT. Figure 5 shows the temperature-dependent electrical conductivity and the Seebeck coefficient of CGT compared to the experimental data reported in Ref. [8]. The temperature dependence of σ and S are similar to that of CZTX. The fitting parameters are listed in Table IV. It should be pointed out that the measured carrier concentration increases rapidly with increasing temperature as shown in the inset of Fig. 5 [8]. We claim that p-type CGT is in the ionization region where hole concentration n has a strong temperature dependence because of the incomplete ionization of doped atoms. The typical expression $n \propto T^{3/4}\exp(-\Delta E_A/2k_BT)$ [49] is employed, where ΔE_A is the acceptor impurity ionization energy which is defined as the difference between acceptor level and VBM.

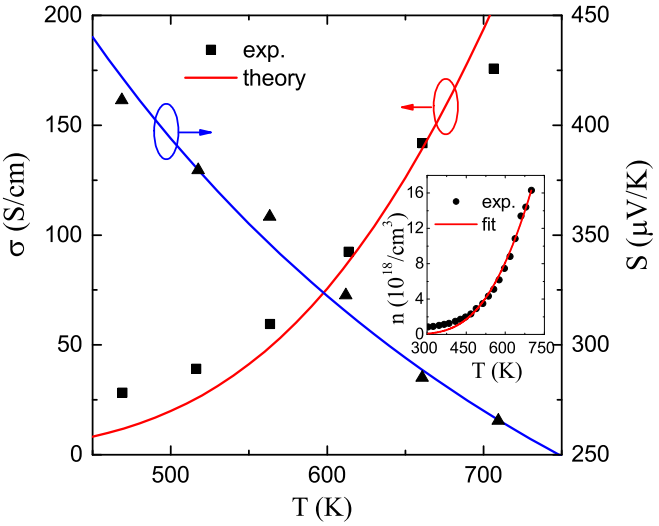

FIG. 5. Calculated electrical conductivity (a) and Seebeck coefficient (b) of CGT as a function of temperature in comparison with the experimental data extracted from Ref. [8]. Inset shows the exponential growth of carrier concentration in comparison with the measured data.

The exact expression is presented in Table IV and the fitting line is shown in the inset of Fig. 5. $\Delta E_A/2k_B = 2427.07$ K is used to calculate the TE transport coefficients, which gives consistent results with Ref. [8]. Other fitting parameters are compared to the references. The optical phonon energy is the same as the experimental values from infrared reflectivity measurement in Ref. [46]. The deformation potential constant is close to the measured value in Ref. [47]. The static and high-frequency permittivities are close to the values calculated from an empirical model [48].

Figures 6(a) and 6(b) show the carrier concentration dependence of σ and S of CBT which is similar to that of CZTX. Figure 6(c) shows the carrier concentration dependence of PF. We find that PF for CGT and CIT are comparable with each other. In the lightly doped region (10^{19} cm^{-3} $< n <$ 10^{20} cm^{-3}), the PF of CGT is slightly larger than that of CIT. In contrast, in heavily doped region, the PF of CIT becomes

TABLE IV. Fitting parameters used to calculate the transport coefficients in CBT. The values in parentheses are the parameters of CIT when they are different from that of CGT.

Parameters	Fitted value	Reference
n (cm^{-3})	$3.84(T/\mathrm{K})^{3/4}e^{-2427.07\,\mathrm{K}/T} \times 10^{18}$	
impurity density (cm^{-3})	4×10^{19}	
mass density (g cm^{-3})	6.03 (4.35)	6.03 (4.35)[a]
optical phonon energy (meV)	24.8	24.8[b]
deformation potential constant (eV)	4.0	4.32[c]
static permittivity (ϵ_0)	13.9	12.7[d]
high-frequency permittivity (ϵ_0)	8.5	8.5[d]
sound velocity (m/s)	3000	

[a]Landolt-Börnstein database.
[b]Reference [46].
[c]Reference [47].
[d]Reference [48].

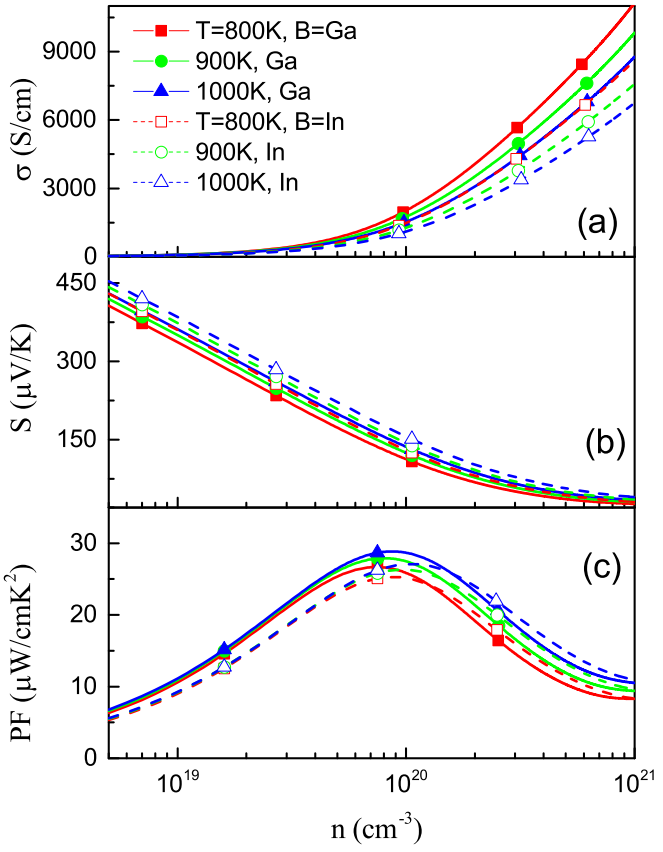

FIG. 6. Calculated electrical conductivity (a), Seebeck coefficient (b), and PF (c) versus carrier concentration in CGT and CIT at $T =$ 800 K, 900 K, 1000 K.

the larger one. The optimal n in CGT is about 8.7×10^{19} cm^{-3} which results in a maximum PF of 28 μW/cm K^2 at 1000 K. For CIT, the optimal n is around 1.1×10^{20} cm^{-3} which results in a maximum PF of 26 μW/cm K^2 at $T = 1000$ K. Compared to the PF of CZTX, the PF of CBT is much larger. Using the thermal conductivity data showing $\kappa \sim 1$ W/mK above 900 K reported in Refs. [7,8], we can expect large ZT above 2 at 900 K.

IV. CONCLUSION

We have incorporated the multiband Boltzmann transport equations with first-principles calculations on electronic band structures in order to theoretically investigate TE properties of quaternary and ternary Cu-based chalcopyrite such as CZTS, CZTSe, CGT, and CIT. Our theoretical calculations are in good agreement with the experimental data with calculated parameters and several other fitting parameters. For quaternary compounds, our results reveal that CZTSe is more competitive as a TE candidate and its optimal carrier concentration is around 5×10^{19} cm^{-3}. For ternary compounds, we have proved that both materials are preferable and their optimal hole concentrations for the best PFs are near 1×10^{20} cm^{-3}. Our comprehensive investigation on these Cu-based TE materials would be useful for exploring practically efficient TE materials.

ACKNOWLEDGMENTS

This work is supported by the National Natural Science Foundation of China (Grant No. 11404244), the Program for New Century Excellent Talents in Universities (Grant No. NCET-13-0431), and the Program for Professor of Special Appointment (Eastern Scholar) at Shanghai Institutions of Higher Learning (Grant No. TP2014012).

[1] F. J. Disalvo, Science **285**, 703 (1999).
[2] L. E. Bell, Science **321**, 1457 (2008).
[3] H. J. Goldsmid and R. W. Douglas, Br. J. Appl. Phys. **5**, 386 (1954).
[4] B. Poudel *et al.*, Science **320**, 634 (2008).
[5] P. Qiu, X. Shi, and L. Chen, Energy Storage Materials **3**, 85 (2016).
[6] X. Shi, L. Xi, J. Fan, W. Zhang, and L. Chen, Chem. Mater. **22**, 6029 (2010).
[7] R. Liu, L. Xi, H. Liu, X. Shi, W. Zhang, and L. Chen, Chem. Commun. **48**, 3818 (2012).
[8] T. Plirdpring, K. Kurosaki, A. Kosuga, T. Day, S. Firdosy, V. Ravi, G. J. Snyder, A. Harnwunggmoung, T. Sugahara, Y. Ohishi, H. Muta, and S. Yamanaka, Adv. Mater. **24**, 3622 (2012).
[9] M. L. Liu, F. Q. Huang, L. D. Chen, and I. W. Chen, Appl. Phys. Lett. **94**, 202103 (2009).
[10] H. Yang, L. A. Jauregui, G. Zhang, Y. P. Chen, and Y. Wu, Nano Lett. **12**, 540 (2012).
[11] C. Sevik and T. Çağın, Phys. Rev. B **82**, 045202 (2010).
[12] F. J. Fan, Y. X. Wang, X. J. Liu, L. Wu, and S. H. Yu, Adv. Mater. **24**, 6158 (2012).
[13] K. Suekuni, H. I. Tanaka, F. S. Kim, K. Umeo, and T. Takabatake, J. Phys. Soc. Jpn. **84**, 103601 (2015).
[14] D. Chen, Y. Zhao, Y. Chen, B. Wang, Y. Wang, J. Zhou, and Z. Liang, ACS Appl. Mater. Interfaces **7**, 24403 (2015).
[15] J. Zhang, R. Liu, N. Cheng, Y. Zhang, J. Yang, C. Uher, X. Shi, L. Chen, and W. Zhang, Adv. Mater. **26**, 3848 (2014).
[16] H. Liu *et al.*, Nat. Mater. **11**, 422 (2012).
[17] Y. He, T. Day, T. Zhang, H. Liu, X. Shi, L. Chen, and G. J. Snyder, Adv. Mater. **26**, 3974 (2014).
[18] R. Chetty, A. Bali, and R. C. Mallik, J. Mater. Chem. C **3**, 12364 (2015).
[19] X. Lu, D. T. Morelli, Y. Xia, F. Zhou, V. Ozolins, H. Chi, X. Zhou, and C. Uher, Adv. Energy Mater. **3**, 342 (2013).
[20] J. Heo, G. Laurita, S. Muir, M. A. Subramanian, and D. A. Keszler, Chem. Mater. **26**, 2047 (2014).
[21] X. Lu, D. T. Morelli, Y. Xia, and V. Ozolins, Chem. Mater. **27**, 408 (2015).
[22] L. D. Zhao, D. Berardan, Y. L. Pei, C. Byl, L. Pinsard-Gaudart, and N. Dragoe, Appl. Phys. Lett. **97**, 092118 (2010).
[23] J. L. Lan, Y. C. Liu, B. Zhan, Y. H. Lin, B. Zhang, X. Yuan, W. Zhang, W. Xu, and C. W. Nan, Adv. Mater. **25**, 5086 (2013).
[24] J. Li, J. Sui, Y. Pei, C. Barreteau, D. Berardan, N. Dragoe, W. Cai, J. He, and L. D. Zhao, Energy Environ. Sci. **5**, 8543 (2012).
[25] J. Sui, J. Li, J. He, Y. L. Pei, D. Berardan, H. Wu, N. Dragoe, W. Cai, and L. D. Zhao, Energy Environ. Sci. **6**, 2916 (2013).
[26] M. K. Balapanov, I. G. Gafurov, U. K. Mukhamed'yanov, R. A. Yakshibaev, and R. K. Ishembetov, Phys. Status Solidi B **241**, 114 (2004).
[27] G. J. Snyder and E. S. Toberer, Nat. Mater. **7**, 105 (2008).
[28] J. Zhou, X. Li, G. Chen, and R. Yang, Phys. Rev. B **82**, 115308 (2010).
[29] G. Kresse and J. Furthmüller, Comput. Mater. Sci. **6**, 15 (1996).
[30] J. P. Perdew, K. Burke, and M. Ernzerhof, Phys. Rev. Lett. **78**, 1396 (1997).
[31] Y. Zhang, J. Zhang, W. Gao, T. A. Abtew, Y. Wang, P. Zhang, and W. Zhang, J. Chem. Phys. **139**, 184706 (2013).
[32] J. Heyd, G. E. Scuseria, and M. Ernzerhof, J. Chem. Phys. **118**, 8207 (2003).
[33] J. Paier, M. Marsman, K. Hummer, G. Kresse, I. C. Gerber, and J. G. Angyán, J. Chem. Phys. **124**, 154709 (2006).
[34] Y. Zhang, X. Yuan, X. Sun, B. C. Shih, P. Zhang, and W. Zhang, Phys. Rev. B **84**, 075127 (2011).
[35] G. Kresse and D. Joubert, Phys. Rev. B **59**, 1758 (1999).
[36] H. J. Monkhorst and J. D. Pack, Phys. Rev. B **13**, 5188 (1976).
[37] C. Persson, B. E. Sernelius, A. F. da Silva, R. Ahuja, and B. Johansson, J. Phys.: Condens. Matter **13**, 8915 (2001).
[38] C. Persson, J. Appl. Phys. **107**, 053710 (2010).
[39] H. R. Liu, S. Chen, Y. T. Zhai, H. J. Xiang, X. G. Gong, and S. H. Wei, J. Appl. Phys. **112**, 093717 (2012).
[40] P. Prabukanthan and R. Dhanasekaran, Mater. Res. Bull. **43**, 1996 (2008).
[41] V. K. Gudelli, V. Kanchana, G. Vaitheeswaran, A. Svane, and N. E. Christensen, J. Appl. Phys. **114**, 223707 (2013).
[42] Y. Pei, X. Shi, A. Lalonde, H. Wang, L. Chen, and G. J. Snyder, Nature (London) **473**, 66 (2011).
[43] B. Nag, *Electron Transport in Compound Semiconductors* (Springer-Verlag, Berlin, 1980).
[44] B. L. Huang and M. Kaviany, Phys. Rev. B **77**, 125209 (2008).
[45] T. Gürel, C. Sevik, and T. Çağın, Phys. Rev. B **84**, 205201 (2011).
[46] V. Riede, H. Sobotta, H. Neumann, H. X. Nguyen, W. Möller, and G. Kühn, Solid State Commun. **28**, 449 (1978).
[47] S. M. Wasim, G. Marcano, and G. S. Pérez, Phys. Status Solidi A **78**, 423 (1983).
[48] R. Márquez and C. Rincón, Phys. Status Solidi B **191**, 115 (1995).
[49] D. Wolpert and P. Ampadu, *Managing Temperature Effects in Nanoscale Adaptive Systems* (Springer, New York, 2012), p. 15.